Oral presentation | Incompressible/compressible/hypersonic flow
Incompressible/compressible/hypersonic flow-V
Fri. Jul 19, 2024 10:45 AM - 12:45 PM Room D

[13-D-04] Exploration of the Influence of Various Backpressure Mechanisms to Inlet Unstart

Jonathan Sosa[1], *Cal Rising[1] (1. U.S. Naval Research Laboratory)

Keywords: Hypersonic, Inlet, Unstart

Twelfth International Conference on
Computational Fluid Dynamics (ICCFD12),
Kobe, Japan, July 14-19, 2024

Exploration of the Influence of Various Backpressure Mechanisms to Inlet Unstart

C. J. Rising* and J. Sosa*
Corresponding author: cal.j.rising.civ@us.navy.mil
* U.S Naval Research Laboratory, Washington, DC, USA

Abstract: In this study, three-dimensional simulations of a single ramp inlet utilizing different backpressure mechanisms at the isolator exit to explore unstart. The mechanisms explored in this paper are flaps to constrict the exit area and a wedge placed centrally to provide flow blockage. Reynolds Averaged Navier Stokes (RANS) simulations are run at varying flap angles and wedge positions to trigger an unstart event. The flap mechanism was found to trigger an unstart event at a smaller contraction ratio than the inlet and was able to sustain a higher pressure ratio. The wedge mechanism was found to unstart the inlet at a smaller contraction ratio due to the strong oblique shocks formed on the leading edge, which interact with the boundary layer. Unsteady Improved Delayed Detached Eddy Simulations (IDDES) are performed for the flap case and were found to show increased separation in the boundary layers as well as a decrease in the supersonic area at the domain exit. These unsteady solutions reveal a fluctuating aerodynamic contraction ratio, which on average is approximately 5% lower than the calculations performed using RANS models.

Keywords: Numerical Algorithms, Computational Fluid Dynamics, Turbulence Modeling.

1 Introduction

Scramjet engines are an attractive air-breathing approach because they employ aerodynamic compression and heating due to intrinsic flow features such as shock waves, rather than relying on rotating mechanical components, such as a compressor, to prepare intake air for efficient combustion. Consequently, no turbine is needed downstream from the combustor to power a compressor, resulting in a very simple engine design with no moving parts within the flow path through the engine. The price of this mechanical simplicity is the need to understand the complex viscous, multi-species, reacting, compressible flow physics in detail throughout the engine in order to ensure that the system design can sustain operation throughout the targeted envelope of flight conditions and maneuvers.

The X-43 and the X-51 programs have been the two successful scramjet flight programs in the U.S. to date. Despite successful flight-tests of the X-43, and X-51 hypersonic vehicles, overcoming engine unstart and combustor flameout is necessary to expand the reliability and operational range of these systems. During unstart the original compression shock system in the inlet and isolator is displaced upstream, often resulting in the formation of a detached shockwave. This can lead to severe unsteady thermal and aerodynamic loads, lower total pressure recovery, reduced air mass capture, combustor flameout and even destruction of the vehicle. In previous flight tests, scramjet unstart has led to several scramjet flight accidents and failures. In 1999 the CIAM/NASA Mach 6.5 flight test faced inlet unstart during the dual mode transition [1, 2]. In 2008, the Australian/U.S. hypersonic initiative, HyCAUSE, failed during flight-testing due to inlet unstart cause by an error in attitude control [3, 4]. Most recently the X-51A flight test [5] faced unstart twice, in 2010 [6], and 2011 respectively [7].

Although the thermodynamic cycle of a scramjet engine is relatively simple and well understood, designing an engine to operate across a large range of flight conditions and vehicle attitudes remains a significant challenge. Experimentally, simulating backpressure to investigate unstart has been typically been approached through some form of mechanical blockage, such as ramps, wedges, or mass flow plugs. There remains the question if for any given geometry if the unstart mechanism experienced by the inlet and isolator is equivalent for a given backpressure through varying backpressure mechanisms. This paper presents the computational investigation of a canonical planar inlet with a constant area isolator driven to

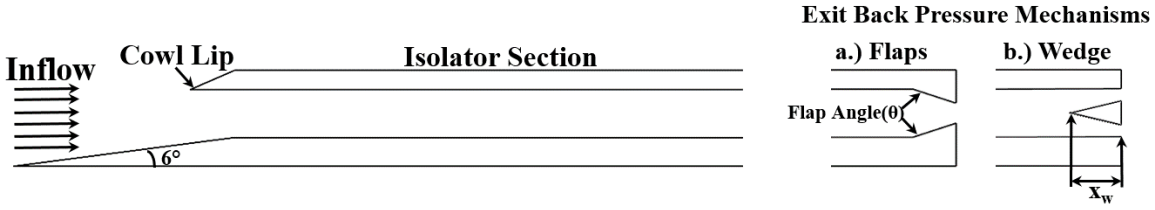

Figure 1: Inlet geometry and back pressure mechanism visualization

unstart though various backpressure mechanisms. The influence of wall bound ramps, backpressure plugs, and fluidic jets to drive up the pressure ratio through the inlet and isolator is investigated in conjunction with the shock train, and shock-boundary layer interactions within the inlet that ultimately lead to inlet unstart. The maximum pressure ratio tolerated for each backpressure mechanisms is cataloged and the boundary layer separation point each unstart event is examined.

2 Problem Statement

In this study, simulations are performed on a single ramp inlet in the Naval Postgraduate School's Mach 4 wind tunnel depicted in Figure 1. The inlet consist of a 6° ramp with length of 90.68 mm which leads into a rectangular isolator section that has a height and width of 15.875 x 38.1 mm and 214.12 is mm long. The freestream conditions into the inlet are a Mach 4 crossflow with a temperature of 69.4 K and pressure of 12.94 kPa.

The primary objective of this study is to investigate the unstart mechanisms which occur due to different backpressure mechanisms implemented experimentally. The first mechanism is flaps placed at the end the isolator section. These flaps are 12.7 mm long and begin parallel to the isolator and are increased to an angle θ to decrease the exit area until an unstart event is triggered. The second method is using a wedge inserted into the center of the isolator at the exit to create backpressure through flow blockage. The length of the wedge is 12.7 mm to maintain consistency with the flap and the half angle of the wedge is set to 10° to provide similar area ratios as the flaps. Preliminary studies were performed and found larger half angles would lead to unstart forming without the wedge fully entering the isolator. Simulations will be performed at different lengths of the wedge inserted into the isolator ranging from x_w = 0 - 12.7 mm.

2.1 Numerical Methods

Three-dimensional numerical solutions of the Reynolds Averaged Navier-Stokes equations are calculated using US3D. A second order accurate Monotonic Upstream-centered Scheme for Conservation Laws (MUSCL) discretization is utilized for the flux extrapolation. The inviscid fluxes are modeled using a Modified Steger-Warming flux vector splitting method. The one equation compressible form of the Spalart-Allmaras model is used to model the Reynolds stresses to close out the RANS equations [8, 9, 10]. Since the RANS model is not valid unless the grid has a near-wall spacing to provide a $y^+ = 1$, implicit time integration is required to allow for less stringent time steps. Therefore for the RANS simulations uses an implicit data-parallel line relaxation (DPLR) method [11]. The CFL is ramped with increasing iterations until a final value of 40, which was found to give the largest time-step while maintaining stability.

Unsteady simulations are performed using an Improved Delayed Detached Eddy Simulation (IDDES) methodology of Shur et. al. to capture the unsteady dynamics of the shock boundary layer interaction and unstart process [12]. The IDDES simulations are computed with a fourth-order-accurate centered kinetic energy consistent (KEC) flux [13]. A second-order-accurate version of an implicit point-relaxation method is used for the implicit time-integration method [14]. The simulations were initialized with the RANS flowfields, and they were run for several domain flowthrough times. A similar CFL was maintained from the RANS simulations and resulted in a timestep of around 30 ns.

2.2 Grid Generation and Convergence

A structured grid was generated using Pointwise[15] grid generation software for the geometry described in Section 2. Clustering was included in the near-wall region to resolve the boundary layer according to a $y^+ = 1$. An initial grid was generated which consisted of approximately 13 million hexahedral elements and shown in Figure 2. A grid refinement study was performed using the RANS simulations on the flap configuration at a constant flap angle of 10° to ensure the mesh captures the pressure increase in the cased of a reduced exit area. The near wall grid spacing was held constant to ensure the RANS model was still accurately implemented and additional resolution was added in the x and z directions. Two additional grids consisting of 21 and 35 million hexahedral elements are tested to measure any influence on the solution.

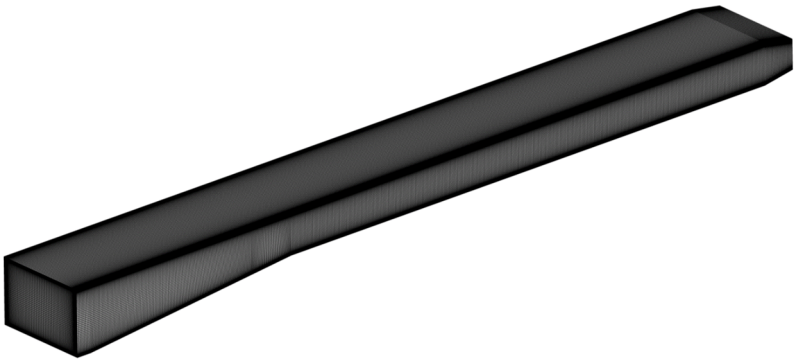

Figure 2: Example structured grid for calculations

Profiles of pressure and velocity from the RANS simulations on each grid are presented in Figure 3. The pressure profiles are extracted along the centerline (z=0) of both the top and bottom walls. The pressure profiles demonstrate that the 13 million mesh is suitable to predict the pressure along the inlet and isolator as there is negligible difference between each grid. Additionally, normalized velocity profiles are extracted along the centerline at an axial location of x = 0.25 m. These profiles also demonstrate similar convergence and that the velocity field is suitably captured by 13 million element mesh.

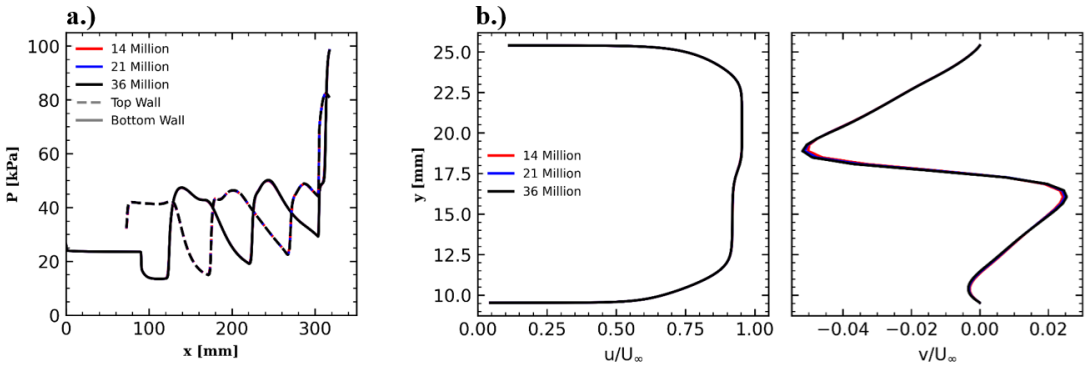

Figure 3: a.) Top and bottom wall pressure profile along inlet centerline and b.) axial (u) and transverse (v) velocity profiles

3 Results

3.1 Flap Back Pressure Mechanism

For this portion of the study the angle of the flap will start at 0° and then increased until an unstart event occurs. The Mach number and pressure distributions along the centerplane at varying flap angle for the steady RANS solutions are presented in Figure 4. The Mach number contours demonstrates the decreasing of speed through the inlet and in the cases of the when the flap angle is increased there is an

increased prevalence of low Mach regions as the flow begins to separate. Similarly the pressure contours demonstrates the pressure increase through the isolator section and the inclusion of the flaps generates a ten times pressure increase near the exit of the domain. It is shown that at a flap angle of 13° that significant backpressure is generated leading to the shock train in the isolator moving upstream and ultimately unstarting the inlet.

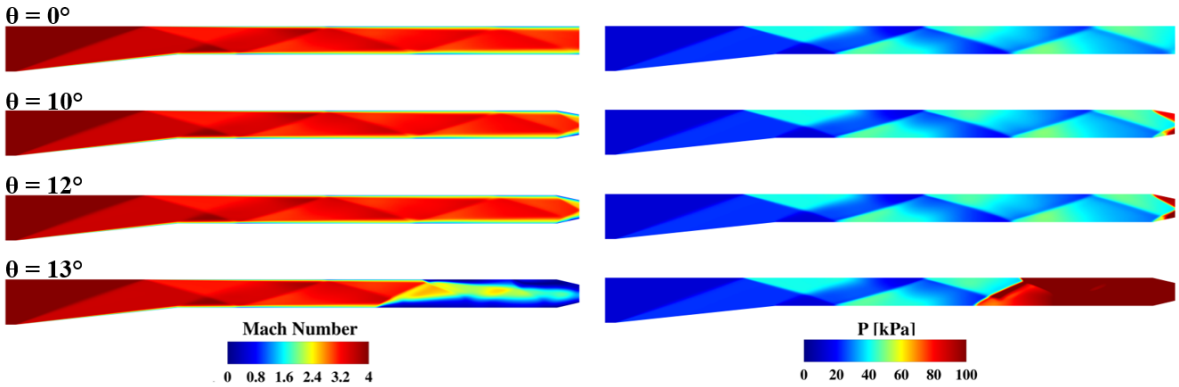

Figure 4: Centerplane Mach number and pressure distribution at varying Flap angles(θ)

To examine the shock structure within the isolator region in more detail, numerical shadowgraph images are generated and presented in Figure 5. It is demonstrated that a shock train forms in the isolator and is generally formed from a series of shock reflections formed from the cowl shock. A weak expansion wave is formed at the ramp end of the inlet ramp but has minimal influence on any shock interactions formed downstream. The inclusion of the flaps forms an additional shock formed from the induced separation of the boundary layer as flow is turned towards the exit. The impingement of a reflected shock from the isolator on the bottom flap, results in a larger separation forming and eventually causing the separation shock to impinge on the top wall. This separation shock formation and movement is directly linked to the unstart process.

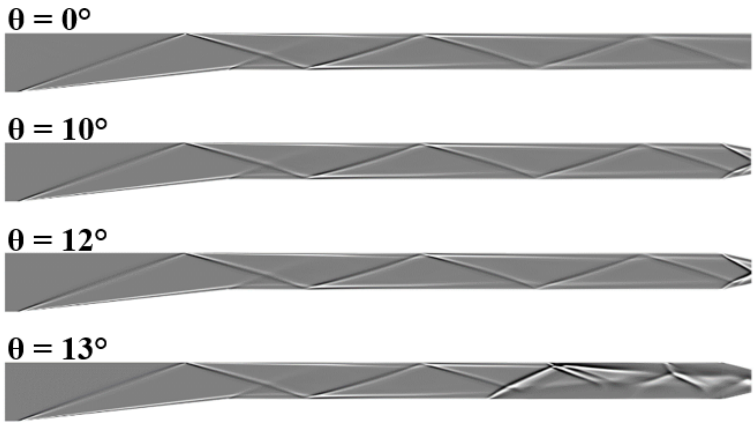

Figure 5: Centerplane numerical shadowgraph distribution at varying Flap angles(θ)

Examining the exit plane of isolator can provide further insight into onset of unstart and local fluid dynamics driving it. The exit plane Mach number is presented in Figure 6 for three flap configurations. As the flap angle is increased, the high Mach region of the core flow begins to decrease in size. Additionally, it is noted that symmetric low Mach zones are found on the top and bottom walls. Along the bottom of the sidewalls it is seen that the subsonic region starts to expand as the flap angle increases until the an unstart event is triggered at $\theta = 13°$. The contour at $\theta = 13°$ is taken at an intermediate step as the exit begins to go subsonic. The driving mechanism, which causes is the large separation zone which occurs emanating from the bottom corners. This region is more prone to separating and dropping to subsonic values at the higher flap angles due to the collision of the boundary layers on the bottom and sidewalls.

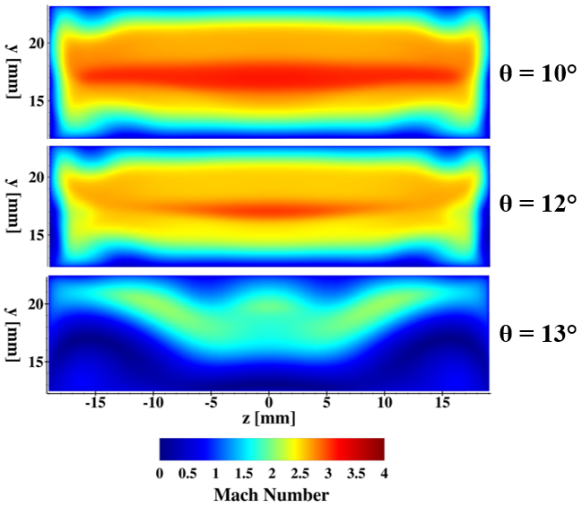

Figure 6: Exit plane Mach number contours at Flap angles of 10-13°

The Kantrowitz diagram is commonly used to depict if an inlet will start or unstart based on the Mach number and the contraction ratio of the inlet. The contraction ratio is defined by the geometric inlet and isolator area, however given that there can be significant boundary layer growth and separation induced from shock boundary layer interactions the aerodynamic area can reduce the effective area. The Kantrowitz diagram is presented in Figure 7 using both the geometric and aerodynamic areas. The aerodynamic exit area is defined as the area at the exit plane that remains supersonic. The Kantrowitz limit is defined as [16]:

$$\left(\frac{A_1}{A_2}\right)_{Kantrowitz} = \left[\frac{(\gamma+1)M_1^2}{2+(\gamma-1)M_1^2}\right]^{(1/2)} \times \left[\frac{(\gamma+1)M_1^2}{2\gamma M_1^2-(\gamma-1)}\right]^{1/(\gamma-1)} \tag{1}$$

The isentropic limit presented on the Kantrowitz diagram is defined as:

$$\left(\frac{A_1}{A_2}\right)_{Isentropic} = \frac{1}{M_1}\left(\frac{\gamma+1}{2}\right)^{-(\gamma+1)/2(\gamma-1)} \times \left(1+\frac{\gamma-1}{2}M_1^2\right)^{(\gamma+1)/2(\gamma-1)} \tag{2}$$

Additionally, previous research by Modler et. al. proposed a startability index S, to be applied to the both Kantrowitz and isentropic limits to determine the limiting contraction ratio [17]. The Molder limit is defined as:

$$CR_{Molder} = \frac{1}{S/CR_{Kantrowitz} + (1-S)/CR_{Isentropic}} \tag{3}$$

The final line provided on the Kantrowitz diagram is an empirical polynomial function proposed by Sun and Zhang which is based on the mass-averaged Mach number at the cowl-lip section [18]. The Sun and Zhang limit is defined as:

$$\left(\frac{A_1}{A_2}\right)_{Sun} = 0.933 + \frac{M_1}{6.87} + \frac{M_1^2}{40.9} \qquad (1.65 \leq M_1 \leq 4.68) \tag{4}$$

In Figure 7, the contraction ratio (CR) is defined based on the inlet inflow area and the internal contraction ratio (ICR) is defined as the area at the cowl lip. It is seen that when considering the geometric ratio all values remain centrally in the dual solution region. Comparing the values of at different angles, there is minimal difference between the 12° and 13° locations but the simulation results reveal that unstart is expected at 13°. When considering the aerodynamic area, the flap angles that remain started only shift slightly downward. However, in the case of the unstarted flow the aerodynamic area shifts the point towards zero and below the isentropic limit. This indicates that the traditional contraction ratio definition may not provide the best representation when considering these experimental unstart

methods.

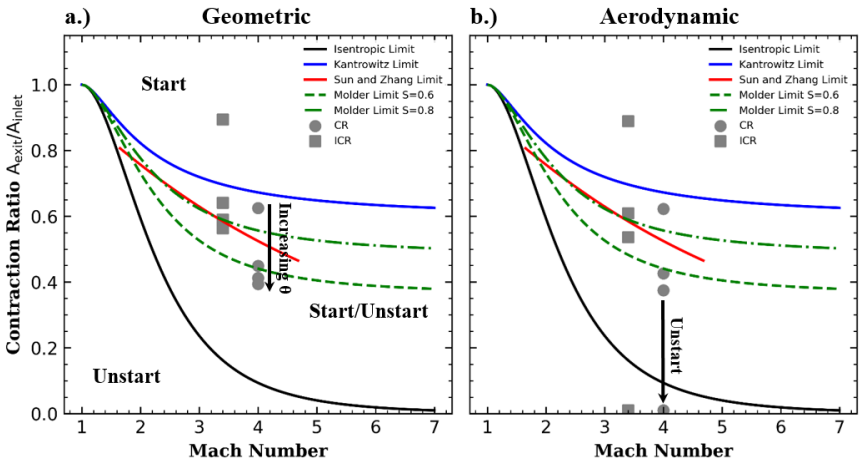

Figure 7: Exit plane Mach number contours at Flap angles of 10-13°

3.2 Wedge Back Pressure Mechanism

The second mechanism examined is the wedge, which is placed centrally in the isolator and slid a distance x_w to incrementally increase the blockage ratio. The Mach number and pressure distributions along the centerplane at increasing x_w for the steady RANS solutions are presented in Figure 8. The primary difference between the wedge and flap mechanism is the generation of a high-pressure region is generated centrally along the wedge as opposed to along the outer wall. Additionally, the wedge generates shocks which begin to interact with the top and bottom walls as x_w is increased. The inlet remain started until the wedge is completely inserted into the isolator, which causes an unstart event to occur.

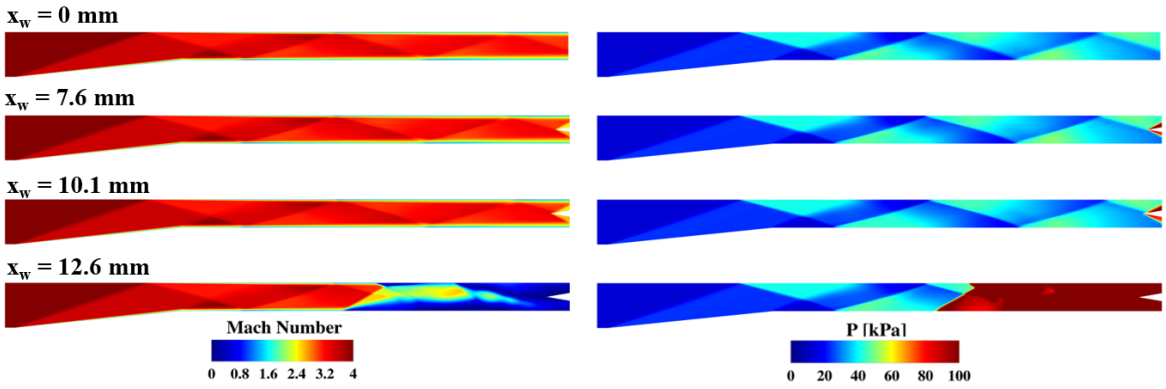

Figure 8: Centerplane Mach number and pressure distribution at varying x_w

To examine the shock structure within the isolator region in more detail, numerical shadowgraph images are generated and presented in Figure 9. The general structures remain identical to the flap configuration in ramp and initial isolator section. As the wedge is moved further into the domain, the reflected shock in the isolator begins to interact with the top wall of the wedge. Eventually the increase shock boundary layer interactions results large pressure increase and unstarts the inlet.

The exit plane Mach number contours are presented in Figure 10. The hashed regions in Figure 10 represent the area taken up by the wedge. It is seen that there are strong corner effects, which result in lower mach regions forming in the corners, with the bottom wall region being influenced more. These corner effects become more pronounced as the wedge is moved to $x_w = 12.7$ and causes the majority of the region below the wedge to become subsonic and eventually push a shocktrain back up the isolator

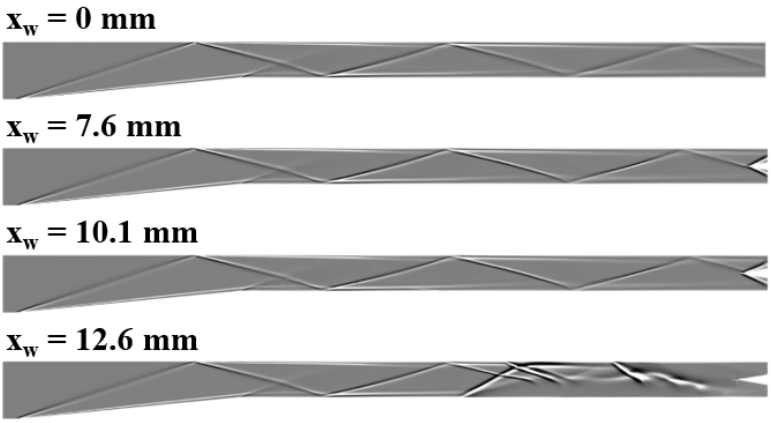

Figure 9: Centerplane numerical shadowgraph distribution at varying x_w

depicted in Figure 9. This asymmetry in the exit plane is similar to the behavior exhibited with the flaps, as the bottom corners were shown to be the driving feature leading to unstart onset. This indicates that regardless of approach the driving mechanism leading to unstart occurring within the isolator remains consistent.

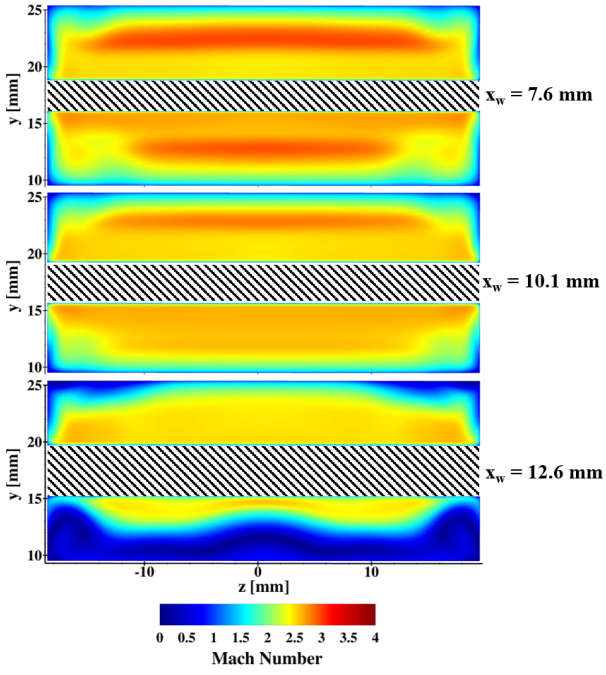

Figure 10: Exit plane Mach number contours at x_w = 7.6 - 12.7mm

Kantrowitz diagrams with the geometric and aerodynamic contraction ratios are presented in Figure 11. Similar to the flaps the geometric solutions primarily lie within the dual solution start/unstart region. When considering the total geometric contraction ratio it is seen that the point where unstart occurs lies approximately along the Molder limit with a coefficient of S = 0.6. This is different from the flap mechanism which lies below the S = 0.6 line and is closer to a coefficient of S = 0.5. The Sun and Zhang limit can only be used for the ICR and does not predict unstart for the wedge mechanism as all points lie above the curve. While this limits that have been determined they may not be able to accurately account for the mechanisms that generate backpressure from the center may require different definitions than those generated along the wall.

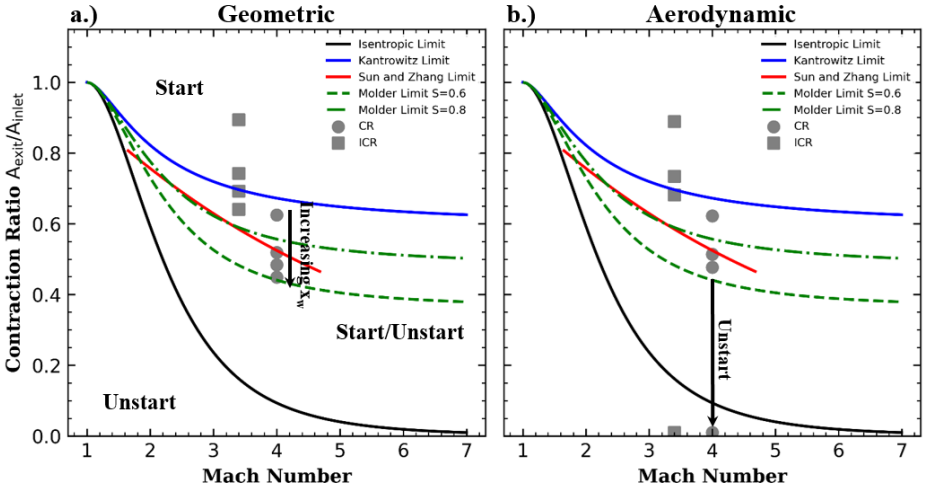

Figure 11: Exit plane Mach number contours at Flap angles of 10-13°

3.3 Comparison of Back Pressure Mechanisms

The results presented in the previous sections revealed that two mechanisms produce different pathways that result in unstart occurring. In Figure 12 a series of images showing the evolution of the unstart event is shown for each mechanism. In the case of the flap mechanism, there is initially a pair of shocks generated from angle change of the flaps. Then the shock from lower flap moves upstream due to separation occurring from the shock boundary layer interaction (SBLI) from the isolator shock train. The separation along the bottom wall continues to grow, driving the separation shock to interact with the top flap.

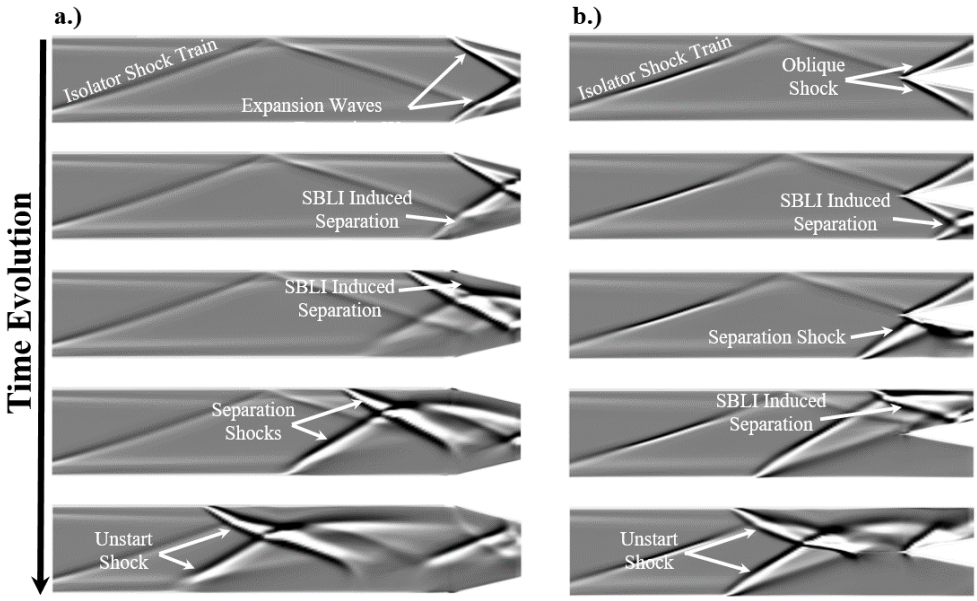

Figure 12: Numerical shadowgraph depicting evolution of unstart event for a.) flap and b.) wedge mechanism

Examining the wedge mechanism in Figure 12b, it is seen that it begins with the oblique shocks forming of the wedge. Along the bottom wall there is a separation shock that forms from the shock boundary layer interaction from the oblique shock off the wedge. This separation continues to move

upstream until the entirety of the area below the wedge becomes subsonic. The separation shock then moves upstream and impinges on the top wall resulting in a reflected shock, which impinges on the top of the wedge. This impingement on the top wall results in subsonic regions appearing in the area above the wedge. Eventually this leads to the two separation shocks forming along the top and bottom wall and lead to the inlet unstarting. The formation of separation shocks on the top and bottom walls leading to unstart is identical for both cases; the stages leading to them forming are different. It is also worth noting that the time scale for unstart occurring in the case of the wedge is approximately twice as fast as the wedge.

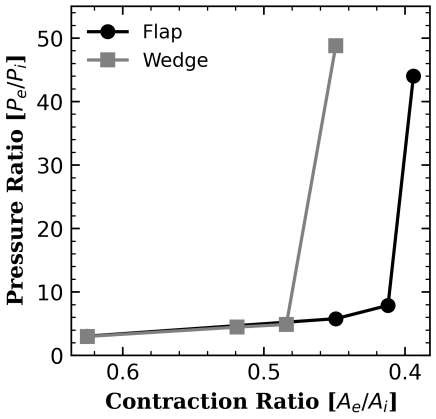

Figure 13: Pressure ratio for both flap and wedge mechanism

For further comparison of the mechanisms, the pressure ratio is calculated at the different flap angles and wedge locations. The pressure ratio is determined by extracting the average value at the exit plane and comparing to the freestream pressure. The pressure ratios are presented at each geometric contraction ratio in Figure 13. The pressure ratios remain nominally constant between the mechanisms until a contraction ratio of 0.48, where the wedge deviates and experiences a 10x increase as the inlet unstarts. The flap mechanism is able to remain started until a contraction ratio 0.4, where the pressure ratio increases by 6x as the inlet unstarts. This highlights the differences in the initiation of the unstart event presented in Figure 12, as the oblique shocks in the wedge develop a larger pressure buildup in the isolator due the shock boundary layer interactions that lead to unstart at larger contraction ratios.

3.4 IDDES Flap Simulations

Unsteady IDDES simulations are run for the wedge mechanism at a flap angle of 10° to determine if there are any differences for a stable case compared to the previously presented RANS simulations. Instantaneous contours of numerical shadowgraph, Mach number, pressure, and vorticty (ω_z) are presented in Figure 14. Noticeable differences are seen in the shadowgraph contour when compared to RANS results in Figure 5. The key differences are the formation of several separation bubbles along the bottom wall, the first of which is generated from the cowl shock. This separation bubble forms an additional shock, which results in several additional separation shocks forming downstream.There are additional separation shocks that interact with the top wall near the exit, however they do not cause significant separation that may lead to inlet unstart.

The Mach number contour depicts that there is a larger low Mach zone within boundary layer region along the top and bottom wall. The shock boundary layer interactions shown in the shadowgraph are seen to continuously increase the low Mach number region along the wall due to the separations that occur. One significant difference between the RANS results is the low Mach number region experienced along the flap walls. In the IDDES simulations the low Mach number region expands upstream of the flap which does not occur in the RANS simulations. Similar trends are shown in the pressure contours, where the pressure along the flap walls is shown to be only high near the exit of the flap. The RANS simulations experienced high pressure along the entirety of the top wall. The final contour in Figure 14 depicts the span-wise vorticity (ω_z) and demonstrates the vorticity development and unsteady behavior experienced due the shock boundary layer interactions along the isolator walls. There is also weak vorticity generation along the shocks that become continuously weaker as they reflect through the

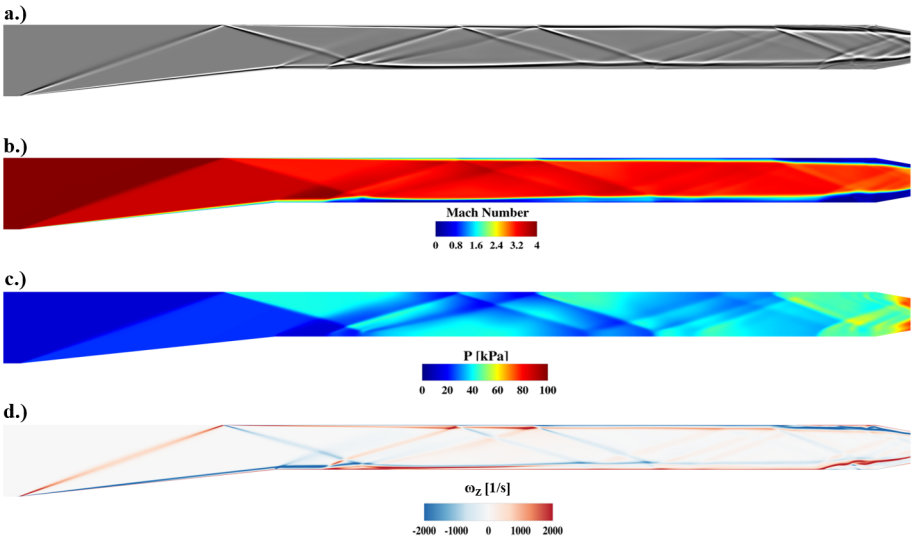

Figure 14: Instantaneous centerplane contours for flap angle $\theta = 10°$ for of a.) numerical shadowgraph b.) Mach number c.) pressure and d.) vorticity (ω_z)

isolator section. The vorticity production becomes strongest once again at the shear region developed along the separation region along the flap.

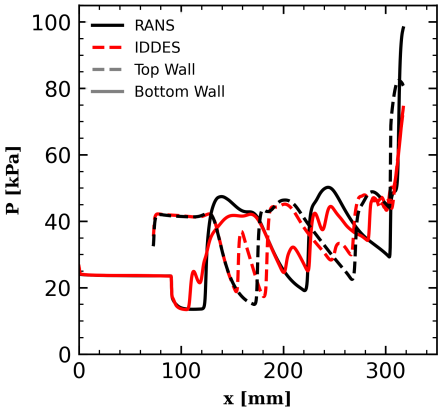

Figure 15: Comparison of top and bottom wall pressure measurements for RANS and IDDES simulations

As another comparison between simulation methods the centerline wall pressure is presented in Figure 15 to further identify any differences between simulation approaches. It is seen that there are additional pressure peaks along the top and bottom walls, which align with regions of shock boundary layer interactions. In general, the peak pressure locations for the IDDES simulations are slightly lower when compared to the RANS measurements. Most notably, the pressure near the exit of the domain reach a lower magnitude in the IDDES than the RANS and are nearly equal, whereas the RANS measurements show an unequal pressure distribution with the top wall reaching a 20% lower overall pressure.

To identify the effects of the low Mach number regions along flaps more closely, an instantaneous contour of the exit Mach number is presented in Figure 16a. It is seen that there are three lobes of low Mach number along the bottom wall along the centerline and at z = +/- 12 mm. These structures indicate that there is streamwise vorticity (ω_x) production generating three counter rotating vortex pairs within the boundary layer. On the top wall, there is no elevated low Mach number region along the centerline. There are however two counter rotating vortex pairs generated near z = +/- 15 mm. This is different from the RANS exit plane, which does not have any significant low Mach number region along the centerline. The off-center low Mach regions are similar to the RANS solution in location but

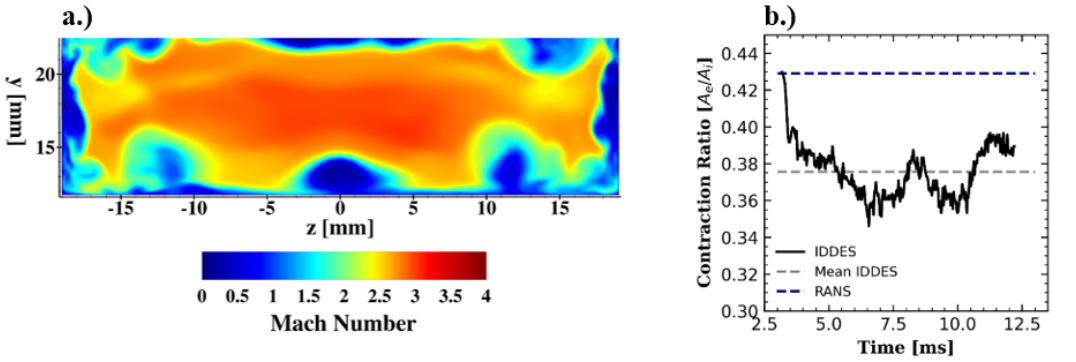

Figure 16: a.) Instantaneous contour of Mach number at the exit plane and b.) Time evolution of aerodynamic contraction ratio

the IDDES has more significant separation along the bottom wall. To compare the supersonic exit area between the simulations, the aerodynamic contraction area is computed through time for the IDDES simulation and presented in Figure 16b. Since the IDDES simulations are initialized from the RANS solution, the initial point represents the contraction ratio for the RANS case. It is seen that in the IDDES the contraction ratio fluctuates as the separation regions on the flaps oscillate through time at approximately every 3 ms between peak contraction ratio values. Extracting the average value from the IDDES results reveals that there is on average an approximately 5% decrease in the aerodynamic contraction ratio compared to the RANS result. While this does not result in unstart occurring it could indicate that the RANS simulations may overpredict the angle at which unstart occurs.

4 Conclusion

In this study three-dimensional simulations of a single ramp inlet with two different back pressure mechanisms are performed. The two mechanisms investigated are flaps angled inwards and a wedge placed centrally within the isolator. RANS simulations were performed and determined the contraction ratio limits that resulted in inlet unstart. It was determined that on the Kantrowitz diagram, the Molder limit with a startability index of S = 0.5-0.6 was found to be reasonably predictive of unstart for both cases. It was determined that the wedge mechanism unstarted at lower contraction ratios due to the strong oblique shock formed off the wedge leading edge. The unstart process was found to be driven by a pair of separation shocks forming on the top and bottom walls.

Unsteady IDDES simulations were also performed to quantify any time-resolved effects present in the unstart process. It was also found that that there is a counter rotating vortex pair found along bottom wall centerline, which does not appear in the RANS simulations. Additionally, the aerodynamic contraction ratio is quantified by extracting the supersonic exit area and it was determined that the IDDES predicts an exit area which is approximately 5% lower. This indicates that RANS simulations may overpredict the contraction ratio where unstart occurs.

References

[1] R Voland, A Auslender, M Smart, A Roudakov, V Semenov, and V Kopchenov. Ciam/nasa mach 6.5 scramjet flight and ground test. In *9th International Space Planes and Hypersonic Systems and Technologies Conference*, page 4848, 1999.

[2] Carlos G Rodriguez. Computational fluid dynamics analysis of the central institute of aviation motors/nasa scramjet. *Journal of Propulsion and Power*, 19(4):547–555, 2003.

[3] Steven Walker and Frederick Rodgers. The hypersonic collaborative australia/united states experiment (hycause). In *AIAA/CIRA 13th International Space Planes and Hypersonics Systems and Technologies Conference*, page 3254, 2005.

[4] Stephen Walker, Frederick Rodgers, Allan Paull, and David Van Wie. Hycause flight test program.

In *15th AIAA International Space Planes and Hypersonic Systems and Technologies Conference*, page 2580, 2008.

[5] Joseph Hank, James Murphy, and Richard Mutzman. The x-51a scramjet engine flight demonstration program. In *15th AIAA international space planes and hypersonic systems and technologies conference*, page 2540, 2008.

[6] Mark Lewis. X-51 scrams into the future. *Aerospace America*, pages 26–31, October 2010.

[7] Guy Norris. X-51a scramjet fails on second attempt. *Aerospace Daily and Defense Report*, June 2011.

[8] Jian Teng and Huacheng Yuan. Variable geometry cowl sidewall for improving rectangular hypersonic inlet performance. *Aerospace Science and Technology*, 42:128–135, 2015.

[9] Huacheng Yuan, Fuzhou Liu, Xin Wang, and Zhenggui Zhou. Design and analysis of a supersonic axisymmetric inlet based on controllable bleed slots. *Aerospace Science and Technology*, 118:107008, 2021.

[10] Yue Zhang, Hui-Jun Tan, Shu Sun, Hao Chen, and Cheng-Hong Li. Experimental and numerical investigation of a fluidically variable hypersonic inlet. *AIAA Journal*, 55(8):2597–2606, 2017.

[11] Michael J Wright, Graham V Candler, and Deepak Bose. Data-parallel line relaxation method for the navier-stokes equations. *AIAA journal*, 36(9):1603–1609, 1998.

[12] Mikhail L Shur, Philippe R Spalart, Mikhail Kh Strelets, and Andrey K Travin. A hybrid rans-les approach with delayed-des and wall-modelled les capabilities. *International journal of heat and fluid flow*, 29(6):1638–1649, 2008.

[13] Pramod K Subbareddy and Graham V Candler. A fully discrete, kinetic energy consistent finite-volume scheme for compressible flows. *Journal of Computational Physics*, 228(5):1347–1364, 2009.

[14] Michael J Wright, Graham V Candler, and Marco Prampolini. Data-parallel lower-upper relaxation method for the navier-stokes equations. *AIAA journal*, 34(7):1371–1377, 1996.

[15] Cadence Design Systems. Pointwise version 2022.1.2.

[16] Arthur Kantrowitz et al. *Preliminary investigation of supersonic diffusers*. National Advisory Committee for Aeronautics, 1945.

[17] Sannu Molder, Evgeny Timofeev, and Rabi Tahir. Flow starting in high compression hypersonic air inlets by mass spillage. In *40th AIAA/ASME/SAE/ASEE Joint Propulsion Conference and Exhibit*, page 4130, 2004.

[18] Bo Sun and Kun-yuan Zhang. Empirical equation for self-starting limit of supersonic inlets. *Journal of Propulsion and Power*, 26(4):874–875, 2010.